pharmaceuticals

MDPI

Article

An Inhalable Asiaticoside-Loaded Liposomal Delivery System Attenuates Pulmonary Fibrosis: Preparation and Efficacy Assessment

Jie Zhang [1,†], Xudong Fan [2,†], XiaoQian Tang [1] and Xinjun Cai [1,2,*]

[1] School of Pharmacy, Zhejiang Chinese Medical University, Hangzhou 310053, China; jiezhang0302@163.com (J.Z.); txq021101@163.com (X.T.)
[2] Department of Pharmacy, Zhejiang Hospital of Integrated Traditional Chinese and Western Medicine, Hangzhou 310003, China; fxd1115@126.com
* Correspondence: zjtcmcxj@zcmu.edu.cn
† These authors contributed equally to this work.

Abstract

Background: Pulmonary fibrosis (PF) is a progressive interstitial lung disease characterized by high mortality rates and limited therapeutic options. Although Asiaticoside (AS) exhibits potent anti-fibrotic activity, its clinical potential is hindered by low bioavailability and insufficient pulmonary targeting. **Methods:** In this study, pH-responsive and charge-tunable AS-loaded liposomes were prepared using the thin-film hydration method and subsequently optimized. The liposomes were characterized in terms of their physicochemical properties, pH-triggered release, stability, and mucus-penetrating capability. Furthermore, cellular uptake by MH-S cells, in vivo biodistribution, and the anti-fibrotic efficacy and safety were evaluated in a bleomycin-induced PF mouse model following pulmonary administration. **Results:** The optimized DPPC-based liposomes exhibited high encapsulation efficiency, excellent stability, pH-dependent drug release, and enhanced mucus penetration with reduced macrophage uptake. These liposomes significantly inhibited fibroblast activation in vitro and attenuated lung injury, collagen deposition, and inflammatory cytokine levels in vivo, demonstrating superior therapeutic efficacy compared to free AS, coupled with a favorable biosafety profile. **Conclusions:** This optimized pH-responsive, pulmonary-targeted liposomal system remarkably enhances the anti-fibrotic efficacy of AS and represents a promising nanodelivery strategy for the treatment of PF.

Keywords: pulmonary fibrosis; asiaticoside; liposomes; pulmonary delivery; mucus penetration

Academic Editors: Nitesh K. Kunda and Serge Mordon

Received: 29 September 2026
Revised: 28 October 2026
Accepted: 3 November 2026
Published: 5 November 2026

Copyright: © 2026 by the authors. Licensee MDPI, Basel, Switzerland. This article is an open access article distributed under the terms and conditions of the Creative Commons Attribution (CC BY) license.

1. Introduction

Pulmonary fibrosis (PF) is a progressive and devastating interstitial lung disease characterized by excessive extracellular matrix deposition, destruction of alveolar architecture, and ultimately respiratory failure [1–3]. Despite significant advances in elucidating its pathogenesis, PF remains associated with a poor prognosis, with a median survival of only 3–5 years following diagnosis, a mortality rate that exceeds that of many malignancies [4,5]. The global burden of PF is steadily increasing, with a rising incidence attributed to aging populations, environmental exposures, and post-viral fibrotic sequelae,

as evidenced by survivors of severe COVID-19 infection [6]. Although pirfenidone and nintedanib are widely used to manage pulmonary fibrosis, their ability to slow disease progression remains limited, and their use may be complicated by gastrointestinal disturbances and liver toxicity. These limitations highlight the need to develop treatments that provide greater therapeutic efficacy with improved safety [7–9].

Pulmonary fibrosis develops through the interaction of ongoing alveolar epithelial damage, abnormal fibroblast responses, and persistent inflammatory activity [10–12]. Transforming growth factor-beta (TGF-β1) serves as the master profibrotic cytokine, driving fibroblast-to-myofibroblast differentiation and excessive collagen synthesis [12–14]. Concurrently, a pro-inflammatory microenvironment characterized by elevated TNF-α and IL-6 perpetuates tissue damage and fibrogenesis [15,16]. Notably, the acidic microenvironment of fibrotic lesions further exacerbates pathological progression and presents both a challenge and an opportunity for targeted drug delivery.

Natural products have emerged as promising sources for anti-fibrotic drug discovery [17]. Asiaticoside (AS), a pentacyclic triterpene saponin derived from the traditional medicinal plant Centella asiatica, has demonstrated potent anti-inflammatory, antioxidant, and anti-fibrotic properties in various disease models [18–20]. However, the clinical translation of AS has been severely hampered by its low bioavailability, rapid systemic clearance, and lack of targeted accumulation at pulmonary lesions [21]. These pharmacokinetic limitations necessitate the development of advanced drug delivery systems capable of overcoming biological barriers and enhancing therapeutic efficacy.

Previous studies have reported asiaticoside-loaded liposomes for non-pulmonary applications, whereas their use for pulmonary diseases, particularly inhaled therapy of pulmonary fibrosis, remains insufficiently investigated [22–25]. Among the various nanocarrier systems explored for pulmonary drug delivery, polymeric nanoparticles, solid lipid nanoparticles (SLNs), extracellular vesicles (EVs), and liposomes have received considerable attention. Polymeric nanoparticles offer tunable physicochemical properties and sustained drug release, while SLNs provide good physical stability and the ability to incorporate poorly water-soluble compounds. EV-based systems exhibit favorable biological properties and intrinsic cellular interactions, but their preparation, characterization, and large-scale production can be challenging. In comparison, liposomes consist of biocompatible phospholipid bilayers and can accommodate both hydrophilic and lipophilic compounds, while their size, surface charge, lipid composition, and PEG modification can be readily adjusted to regulate drug release, mucus interactions, and cellular uptake. These properties make liposomes an attractive platform for pulmonary delivery of AS. Importantly, liposomes can be engineered with tailored surface charge and polyethylene glycol (PEG) modification to optimize mucus penetration, cellular internalization, and pulmonary accumulation [26–28]. The pulmonary administration route offers distinct advantages for PF treatment, including direct delivery to the lungs, reduced systemic exposure, and improved patient compliance [29–32]. Nevertheless, the pulmonary mucus layer and alveolar macrophage clearance present important barriers that necessitate rational design of nanocarrier physicochemical properties [31–33].

The fibrotic lung microenvironment exhibits unique pathological features, including acidic pH, elevated reactive oxygen species, and dense extracellular matrix, which can be exploited for stimuli-responsive drug release [34]. pH-responsive nanocarriers have shown particular promise, as the acidic fibrotic microenvironment (pH 5.5–6.5) differs substantially from physiological pH 7.4, enabling targeted drug release at diseased sites [35–37]. Furthermore, the surface charge of nanocarriers critically influences their interaction with biological components, mucus penetration capacity, and cellular uptake efficiency [38–40]. However, the specific contribution of individual lipid components to the pH-responsive release of AS-loaded liposomes remains unclear. Therefore, in this study,

we compared DPPC-, DPPG-, and DOTAP-based liposomes to investigate their pH-dependent drug release behavior and identify the formulation with the most pronounced pH responsiveness.

Despite advances in liposomal pulmonary drug delivery, the influence of lipid composition on the balance between mucus penetration and macrophage uptake and its implications for the pulmonary delivery of asiaticoside (AS) remain insufficiently understood. In particular, the relationship between these formulation-dependent properties and the subsequent anti-fibrotic effects of AS requires further investigation. To address this gap, the present study compared DPPC-, DPPG-, and DOTAP-based liposomes and evaluated their physicochemical properties, drug-release behavior, mucus penetration, and macrophage uptake. The selected formulation was further investigated for pulmonary distribution and anti-fibrotic efficacy in vitro and in a bleomycin-induced mouse model of pulmonary fibrosis. This integrated evaluation provides a basis for understanding how lipid composition influences the delivery-related properties and therapeutic potential of inhalable AS-loaded liposomes.

2. Results

2.1. Characterization and TEM of AS@Liposomes

In this study, the physicochemical properties of asiaticoside (AS) liposomes constructed with three different phospholipids (AS@Liposomes-DPPC, AS@Liposomes-DPPG and AS@Liposomes-DOTAP) were characterized according to the formulation ratios from A0 to A5 (Figure S1). The encapsulation efficiency (EE%) and drug loading (DL%) values determined for the three types of phospholipids and their respective A0–A5 ratios are presented in Table S2. The optimal formulation for each of the three phospholipids was selected using encapsulation efficiency and drug loading as reference factors. Taking both encapsulation efficiency and drug loading into account, the principle of prioritizing encapsulation efficiency was adopted for the results based on these data; the selected formulations were DPPC-A5, DPPG-A5, and DOTAP-A5, each with a cholesterol-to-DSPE-PEG2000 mass ratio of 1:1. Furthermore, the EE% values for DPPC-A5, DPPG-A5, and DOTAP-A5 were 31.68 ± 0.773, 20.60 ± 0.856, and 18.14 ± 2.729, respectively, while the corresponding DL% values were 3.04 ± 0.982, 2.79 ± 0.311, and 2.83 ± 0.139. The kinetic parameters for the release profiles are provided in Supplementary Table S1. The Korsmeyer–Peppas exponent values (n = 0.203–0.327) suggest a substantial contribution of diffusion to AS release. As shown in Figure 1A, the average particle sizes of the three liposomes were approximately 194.7 ± 4.2 nm, 154.3 ± 5.1 nm, and 138.2 ± 3.6 nm. The polydispersity index (PDI) ranged from 0.12 to 0.21, demonstrating good particle size uniformity. Zeta potential results (Figure 1B) showed that DPPC and DPPG liposomes carried negative surface charges (−33.2 ± 2.4 mV and −35.7 ± 1.9 mV, respectively), while DOTAP liposomes carried a positive surface charge (+32.4 ± 3.1 mV). Transmission electron microscopy (TEM) images (Figure 1C) further confirmed that DPPC and DPPG liposomes were regularly spherical with a uniform size distribution, consistent with the dynamic light scattering (DLS) results. In contrast, DOTAP liposomes presented irregular and aggregated morphologies, which might be related to their positive surface charge and interparticle interactions.

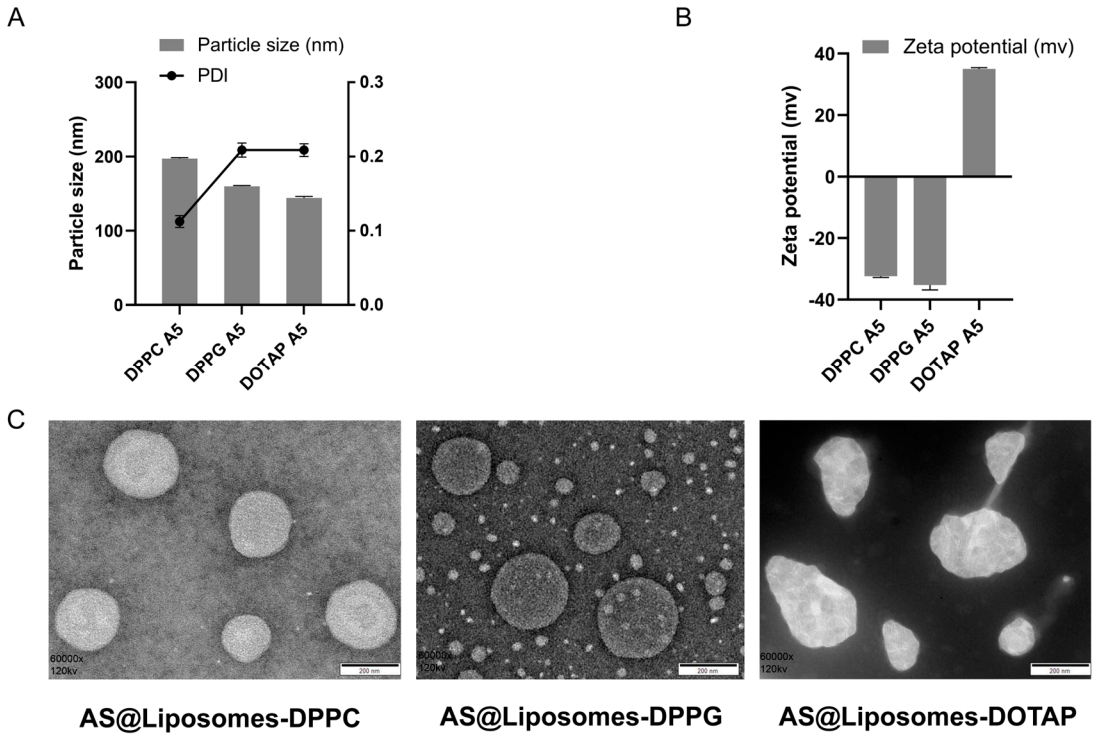


Figure 1. Characterization of optimal AS–loaded liposome formulations. (**A**) Particle size and PDI; (**B**) zeta potential; (**C**) TEM images of DPPC–, DPPG–, and DOTAP–based liposomes. Scale bars = 200 nm.

2.2. Storage Stability

To investigate the stability of the preparations, the particle size, dispersion coefficient (PDI), and surface potential of the blank liposomes and the three phospholipid-constructed asiaticoside-loaded liposomes were measured for 7 consecutive days. The results indicated that the DPPC group performed very stably as a whole; whether for blank or drug-loaded liposomes, the particle size hardly fluctuated for an entire week. The PDI remained stable around 0.2, and the potential was firmly maintained between −13 and −16 mV, suggesting that even after encapsulating the drug, the original structure and state of the liposomes were not disrupted at all (Figure 2A). As for the DPPG anionic liposomes, the particle size was very stable throughout the process. Although the PDI had slight fluctuations, it never exceeded 0.3, and the dispersion was still qualified (Figure 2B). However, the potentials of both groups gradually became more negative with storage time, and at the same time point, the negative charge of the drug-loaded liposomes was always slightly stronger than that of the blank group. Nevertheless, the stability of the cationic DOTAP system was weaker compared to the former two (Figure 2C). Within a week, both particle size and PDI increased slowly and slightly, and the positive surface potential also increased gradually. Interestingly, encapsulating asiaticoside could slightly moderate this change, as the particle size, PDI, and potential values of the drug-loaded group were slightly lower each day than those of the blank DOTAP liposomes at the same time.

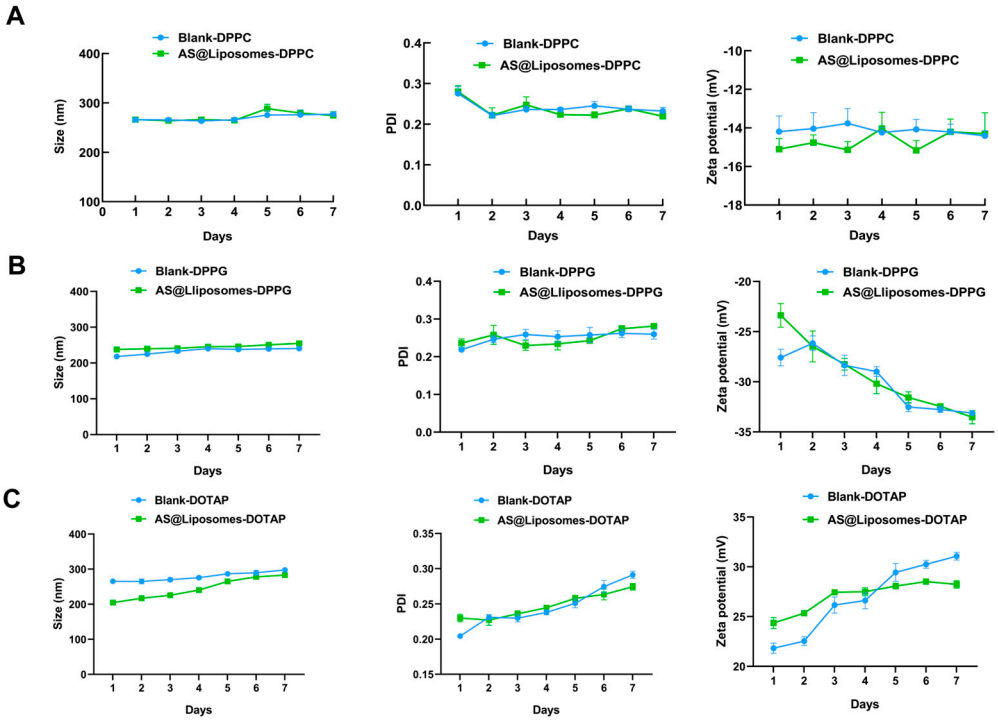


Figure 2. Storage stability of blank and AS-loaded liposomes. (**A**–**C**) Changes in particle size, PDI, and zeta potential of DPPC– DPPG–, and DOTAP–based liposomes over 7 days.

2.3. In Vitro Release Characteristics

The in vitro release profiles of AS from the three liposomal formulations were evaluated at pH 7.4 and pH 5.5 (Figure 3A–C). All three formulations exhibited pH-dependent drug release, with higher cumulative AS release at pH 5.5 than at pH 7.4. The release profiles showed an initial rapid-release phase during the first 12 h, followed by a slower and sustained-release phase. Among the three liposome formulations, DPPC liposomes showed a more obvious difference in the cumulative release of AS at pH 5.5 compared with pH 7.4, suggesting that it has a more obvious pH-dependent release characteristic. Because the release study involved serial sampling from the same release system, the triplicate measurements were considered technical replicates, and statistical comparisons between the complete release profiles were therefore not performed.

To further characterize the release kinetics, the release data were fitted using zero-order, first-order, Higuchi, and Korsmeyer–Peppas models (Table 1). The Korsmeyer–Peppas model yielded n values of 0.203–0.327, suggesting that Fickian diffusion contributed substantially to AS release. The DPPC-based liposomes showed significantly higher AS release at pH 5.5 than at pH 7.4, indicating pH-dependent release behavior. However, the data do not establish a specific active pH-triggered mechanism, and the observed pH dependence may involve both diffusion and changes in membrane permeability.

The results of the in vitro pulmonary mucus penetration experiment are shown in Figure 3D. Free ASiaticoside (free AS) could hardly penetrate the mucus barrier, and the overall penetration rate remained at a very low level within 24 h. The mucus penetration abilities of the three liposomes were all significantly better than that of the free drug. Quantitative results showed that AS@Liposomes-DPPC had the highest mucus penetration rate and final cumulative penetration rate, followed by AS@Liposomes-DPPG, and the cationic AS@Liposomes-DOTAP had the lowest mucus penetration efficiency among the three groups.

Table 1. Primer sequences and theoretical amplification length.

Genes		Primer Sequences (5′-3′)	Product Size (bp)
Acta2	Forward	GTCCCAGACATCAGGGAGTAA	134
	Reverse	TCGGATACTTCAGCGTCAGGA	
Col1a1	Forward	GCTCCTCTTAGGGGCCACT	103
	Reverse	CCACGTCTCACCATTGGGG	
Fn1	Forward	ATGTGGACCCCTCCTGATAGT	124
	Reverse	GCCCAGTGATTTCAGCAAAGG	
GAPDH	Forward	TGTGTCCGTCGTGGATCTGA	138
	Reverse	TTGCTGTTGAAGTCGCAGGAG	

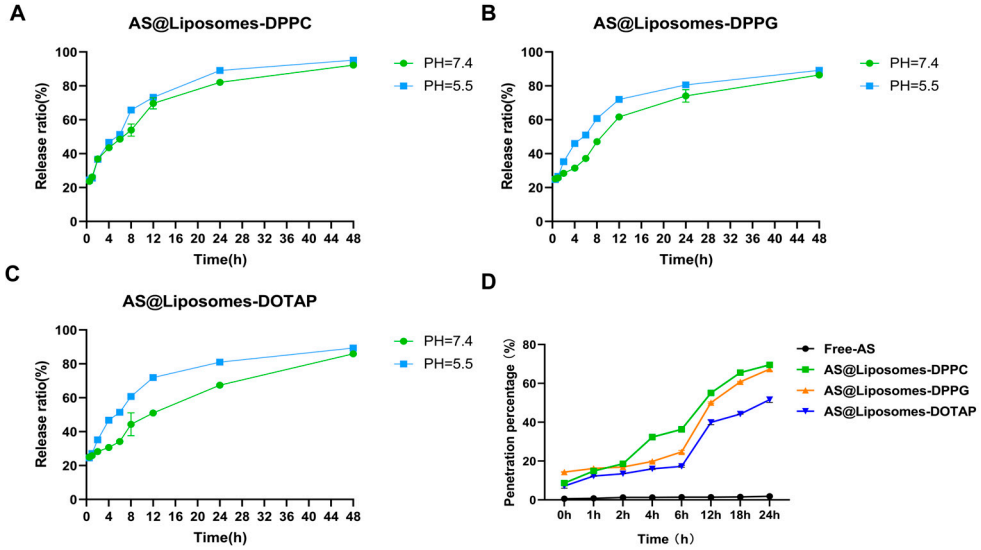


Figure 3. In vitro release and mucus penetration of AS-loaded liposomes. (**A**–**C**) pH-dependent release profiles of DPPC, DPPG, and DOTAP liposomes. (**D**) Pulmonary mucus penetration of different formulations over 24 h.

2.4. Cellular Uptake

Taking MH-S mouse alveolar macrophages as the cellular uptake model, free ASiaticoside and drug-loaded liposomes constructed by three phospholipids were traced by ICG fluorescence. Combined with confocal laser qualitative imaging and intracellular mean fluorescence intensity quantitative detection, the differences in phagocytosis of different lipid carriers by alveolar macrophages were explored to screen for a delivery system with pulmonary immune evasion potential. Confocal imaging results (Figure 4A) showed that the intracellular green fluorescence signal intensity of each group gradually increased with the extension of incubation time, proving that the phagocytosis of macrophages in various preparations was time-dependent. Under the same incubation duration, only weak green fluorescence signals could be observed inside the cells in the AS@DPPC-ICG treatment group; the intracellular fluorescence signal of the free ICG group was slightly higher than that of AS@DPPC-ICG; the intracellular fluorescence signal significantly increased after the AS@DPPG-ICG treatment; and a large amount of intracellular fluorescence accumulation could be observed in cells treated with AS@DOTAP-ICG. The quantitative statistical results of intracellular mean fluorescence intensity (Figure 4B) were consistent with the microscopic observation results. At each incubation time point, the intracellular fluorescence intensity of the AS@DPPC-ICG group was at a low level, showing statistical differences from the other two liposome treatment groups. As the incubation time extended from 1 h to 4 h, the intracellular fluorescence intensity of all groups rose to

different extents, and the cationic liposome group had the most obvious increase in fluorescence signal. The above results suggest that using DPPC as a carrier can reduce the possibility of recognition and phagocytosis by alveolar macrophages and improve the concentration of drugs reaching the target site.

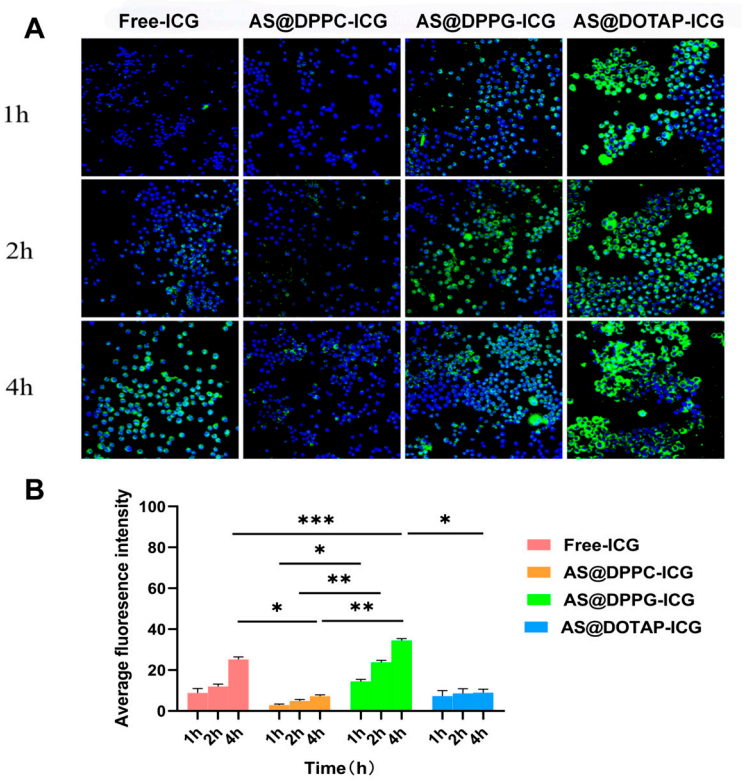


Figure 4. Cellular uptake of different formulations in MH-S mouse alveolar macrophages. (**A**) Confocal laser scanning microscopy (CLSM) images showing the internalization of free ICG (Free-ICG), AS@DPPC-ICG, AS@DPPG-ICG, and AS@DOTAP-ICG by MH-S cells after incubation for 1, 2, and 4 h. Blue fluorescence represents nuclei stained with DAPI, and green fluorescence represents ICG-labeled formulations. (**B**) Quantitative analysis of the average intracellular fluorescence intensity of ICG in MH-S cells after treatment with different formulations for 1, 2, and 4 h.* $p < 0.05$, ** $p < 0.01$, and *** $p < 0.001$.

2.5. Inhibition of Fibroblast Wound Closure

The anti-fibrotic effects of free AS and DPPC-based AS-loaded liposomes (DPPC-AS@Liposomes) were further evaluated using a scratch wound healing assay. Compared with the TGF-β1 model group, free AS moderately inhibited wound closure, whereas DPPC-AS@Liposomes produced a more pronounced inhibition at both 24 and 48 h (Figure 5A). Quantitative analysis confirmed that the wound closure rate was significantly lower in the DPPC-AS@Liposomes group than in the free AS group (Figure 5B), suggesting that liposomal encapsulation enhanced the inhibitory effect of AS on TGF-β1-induced wound closure. However, as cell proliferation was not independently inhibited or assessed, the observed changes may reflect contributions from both cell migration and proliferation.

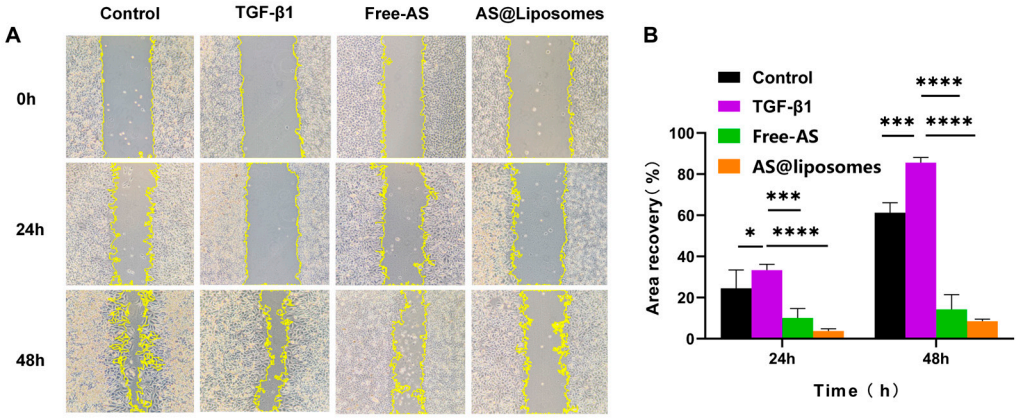


Figure 5. Effects of DPPC-AS@Liposomes on fibroblast migration in a TGF-β1-induced wound healing model. (**A**) Representative images of the wound healing assay at 0, 24, and 48 h. (**B**) Quantitative analysis of wound area recovery at 24 and 48 h. Data are presented as mean ± SD. Statistical significance was determined using one-way ANOVA followed by Tukey's multiple comparisons test. * $p < 0.05$, *** $p < 0.001$, and **** $p < 0.0001$.

2.6. AS@Liposomes Attenuated TGF-β1-Induced Fibrotic Responses in L929 Fibroblasts

To further evaluate the anti-fibrotic effect of AS@Liposomes, L929 fibroblasts were stimulated with TGF-β1 to establish an in vitro fibrosis model. Western blot analysis (Figure 6A) showed that TGF-β1 stimulation markedly increased the protein expression of collagen I and α-SMA compared with the control group. Quantitative analysis (Figure 6B, C) further confirmed the significant upregulation of collagen I and α-SMA following TGF-β1 stimulation. Treatment with free AS partially reduced the expression of these fibrosis-associated proteins, whereas AS@Liposomes produced a more pronounced inhibitory effect. Consistent with the protein expression results, RT-qPCR analysis (Figure 6D–F) demonstrated that TGF-β1 stimulation increased the mRNA levels of Fn1, Col1a1, and Acta2, while treatment with AS@Liposomes significantly suppressed the expression of these fibrosis-related genes. Compared with free AS, AS@Liposomes exhibited a stronger inhibitory effect on both protein and mRNA levels of fibrosis-associated markers. Collectively, these results demonstrate that AS@Liposomes effectively attenuated TGF-β1-induced fibrotic responses in L929 fibroblasts.

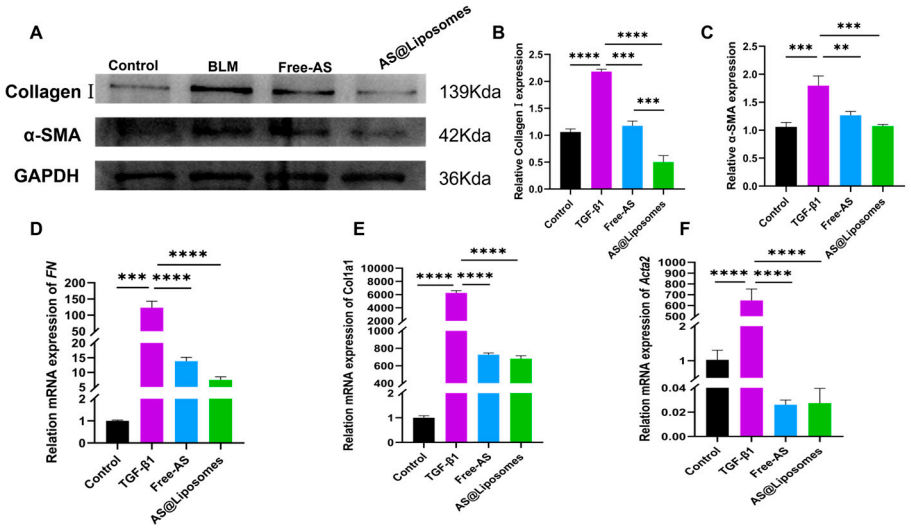


Figure 6. Effects of DPPC-AS@Liposomes on fibrosis-associated protein and gene expression. (**A**) Representative Western blot images of collagen I, α-SMA, and GAPDH in the indicated groups. (**B**)

Quantitative analysis of collagen I protein expression. (**C**) Quantitative analysis of α-SMA protein expression. (**D**) Relative mRNA expression of Fn1. (**E**) Relative mRNA expression of Col1a1. (**F**) Relative mRNA expression of Acta2. Data are presented as mean ± SD. Statistical significance was determined using one-way ANOVA followed by Tukey's multiple comparisons test. ** $p < 0.01$, *** $p < 0.001$, and **** $p < 0.0001$.

2.7. Biodistribution

To investigate the in vivo biodistribution of AS@liposomes, researchers administered ICG-labeled free AS or AS@liposomes to mice via intratracheal instillation and performed ex vivo fluorescence imaging of major organs 24 h later. In a separate experiment, C57 mice were administered free AS or AS@liposomes intratracheally; they were sacrificed 24 h post-administration, and major organs were harvested for LC-MS/MS analysis. As shown in Figure 7, fluorescence imaging revealed significant differences in the distribution patterns of free AS and AS@liposomes across major organs, including the heart, liver, spleen, kidneys, and lungs (A, B). Notably, AS@liposomes exhibited a stronger fluorescence signal in the lungs compared to free AS. The LC-MS/MS results (C) were consistent with the fluorescence imaging findings, demonstrating that AS concentrations in the lungs were higher in the AS@liposome group than in the free AS group, whereas AS levels in other major organs were relatively low. These results indicate that intratracheal administration of AS@liposomes promotes AS accumulation in the lungs and enhances lung-targeting distribution.

2.8. In Vivo Therapeutic Efficacy

A mouse pulmonary fibrosis model was induced by bleomycin (BLM) to comprehensively evaluate the anti-fibrotic effects of free AS and AS@Liposomes at three levels: overall survival status of animals, the inflammatory regulation level, and lung tissue pathological injury. Body weight monitoring showed that the body weight of the model group decreased continuously; the weight loss in the free AS group was reduced, while the AS@Liposomes group had the best weight maintenance effect (Figure 8A). The BALF of each group was analyzed by ELISA kits. The results showed that the secretion levels of two pro-inflammatory cytokines, TNF-α and IL-6, rose significantly in the BLM model group, suggesting that lung inflammation was largely activated. Free ASiaticoside could down-regulate the expression of inflammatory factors; the decrease in inflammatory factor concentration in the bronchoalveolar lavage fluid was more significant after AS@Liposomes intervention (Figure 8B), and the differences between groups were statistically significant. Lung tissue sections of mice in each group were collected for histopathological detection. HE staining showed that the blank group had complete alveolar structures and no obvious inflammatory cell infiltration; the BLM model group showed large-area alveolar collapse and thickened alveolar septa, and the pulmonary interstitium was filled with a large number of inflammatory cells; the free ASiaticoside treatment could mildly alleviate pulmonary inflammatory infiltration and structural destruction; the alveolar morphology in the AS@Liposomes group was better retained; and the degree of inflammatory infiltration was significantly reduced. Masson collagen staining indicated that the blank group had only a small amount of collagen around blood vessels and airways; the BLM model group showed a wide range of blue-stained collagen deposition in the lung interstitium, and the fibrotic lesions were severe. Free ASiaticoside could reduce the collagen accumulation area, and AS@Liposomes could significantly inhibit the abnormal deposition of interstitial collagen and delay the process of lung tissue fibrotic remodeling, showing that AS@Liposomes can significantly improve the overall therapeutic effect of asiaticoside on pulmonary fibrosis (Figure 8C).

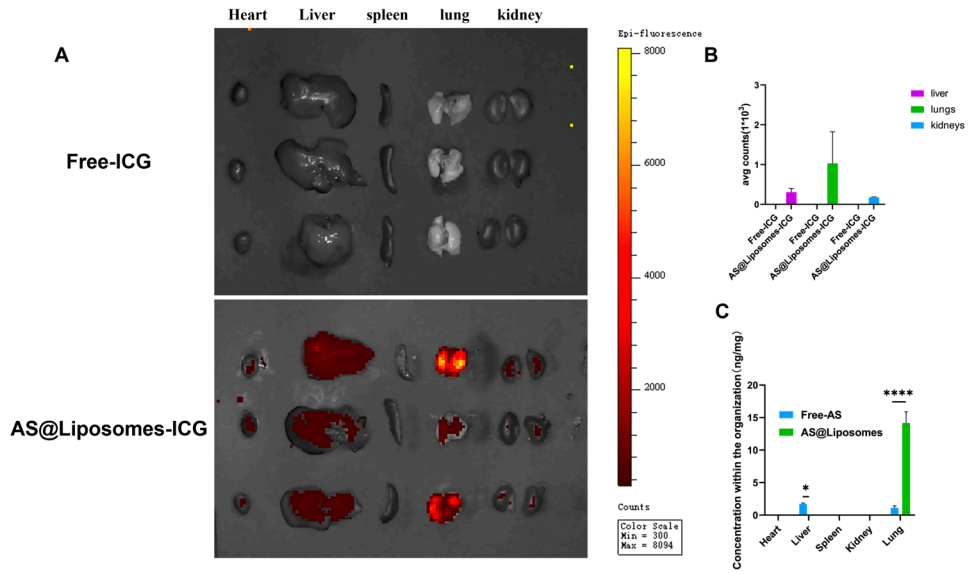


Figure 7. Biodistribution of free AS and AS@liposomes in major organs. (**A**) Representative ex vivo fluorescence images of major organs (including heart, liver, spleen, kidneys, and lungs) collected after intratracheal administration of free AS and AS@liposomes. (**B**) Corresponding fluorescence intensity images showing the distribution of fluorescence signals in the excised organs. (**C**) Quantitative results of AS concentrations in major organs (including heart, liver, spleen, kidneys, and lungs) determined by LC-MS/MS. Data are expressed as mean ± standard deviation (SD). * $p < 0.05$, and **** $p < 0.0001$.

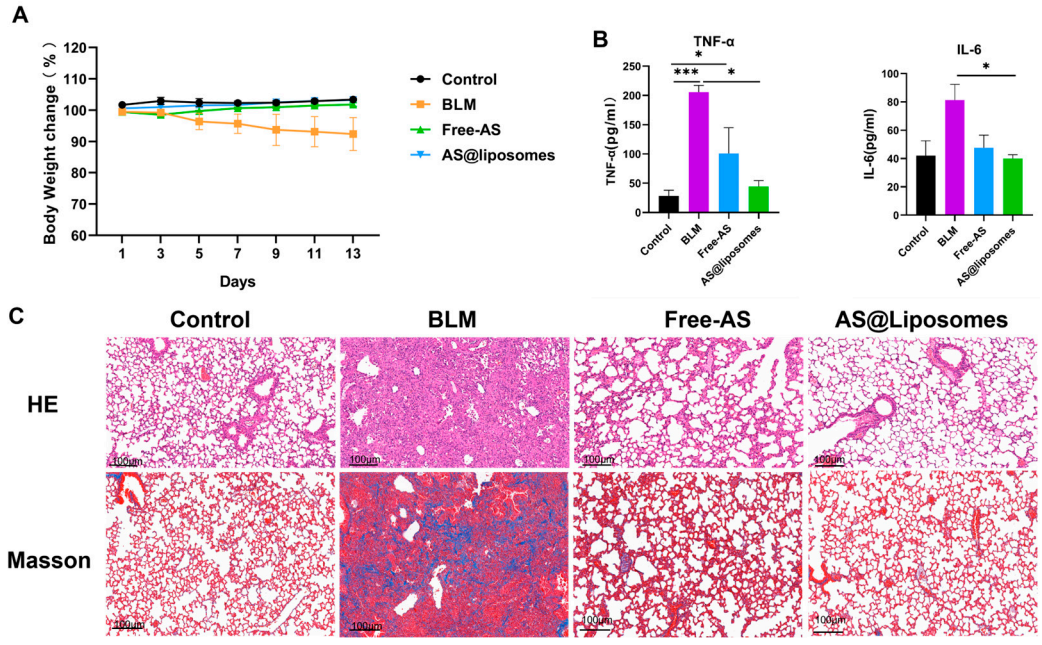


Figure 8. In vivo therapeutic efficacy of asiaticoside liposomes in a bleomycin (BLM)-induced pulmonary fibrosis mouse model. (**A**) Body weight change (%) of mice in the control, model (BLM), free AS, and AS@Liposomes groups over 13 days. (**B**) Levels of pro-inflammatory cytokines TNF-α and IL-6 in bronchoalveolar lavage fluid (BALF) of different groups, measured by ELISA. **(C)** Representative histopathological images of lung tissue sections stained with hematoxylin and eosin (HE, upper row) and Masson's trichrome (lower row) for each group (scale bar: 100 μm). * $p < 0.05$, and *** $p < 0.001$.

2.9. Biosafety Evaluation

To evaluate the in vivo biosafety of AS@Liposomes, histological analysis of major organs and serum biochemical assays were performed. H&E staining of the heart, liver, spleen, and kidneys showed no obvious pathological damage in all groups (Figure 9A). Liver function indicators (ALT and AST) and renal function indicators (BUN and CREA) showed no significant differences among groups (Figure 9B), with all values within the normal physiological range. These results indicate that AS@Liposomes exhibit good in vivo biosafety with no obvious toxicity to major organs at the experimental dose.

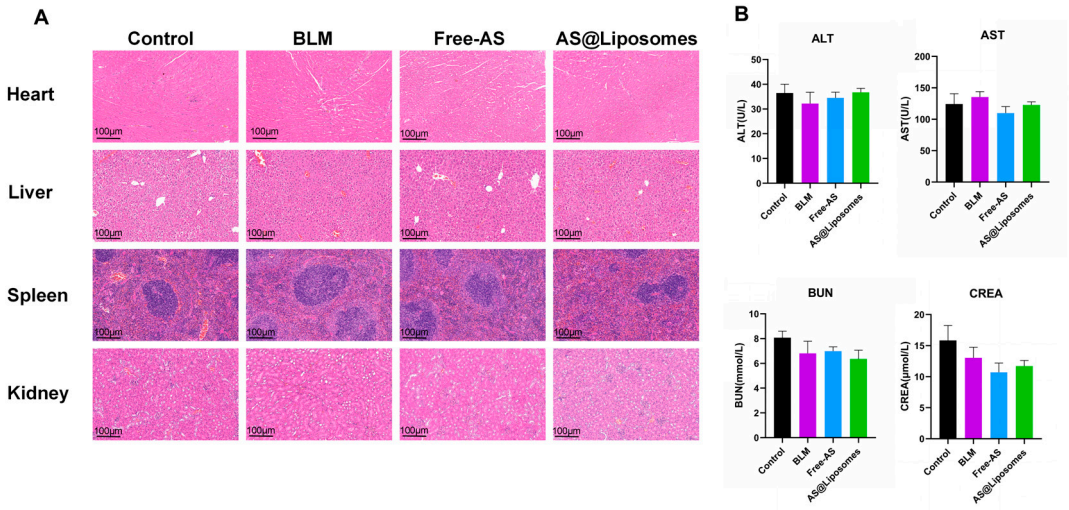


Figure 9. Biosafety evaluation of the formulations in mice. (**A**) H&E staining of major organs (heart, liver, spleen, kidneys) in different groups (scale bar: 100 μm). (**B**) Serum biochemical indicators of liver function (ALT, AST) and renal function (BUN, CREA).

3. Discussion

In the present study, we developed an asiaticoside (AS)-loaded liposomal delivery system for pulmonary fibrosis and systematically compared DPPC-, DPPG-, and DOTAP-based formulations. Differences in lipid composition and surface properties were associated with distinct mucus penetration, macrophage uptake, and drug-release behaviors. Among the tested formulations, the DPPC-based liposomes exhibited favorable mucus penetration together with relatively low macrophage uptake and were therefore selected for subsequent therapeutic evaluation. These findings underscore the importance of balancing mucus transport and cellular clearance when designing liposomal carriers for pulmonary drug delivery. Although DPPC-based liposomes exhibit excellent mucus-penetrating capabilities and low macrophage uptake, their impact on delivery to fibroblasts and their role in macrophage-mediated inflammatory responses remain unclear. The aggregation of DOTAP liposomes, as observed via transmission electron microscopy (TEM), may affect the dispersion state of the particles; however, the stability of these liposomes in suspensions or serum was not evaluated in this study. Furthermore, the artificial mucus model employed fails to fully replicate the characteristics of native pulmonary mucus, and its viscosity has not been sufficiently characterized. Future research should utilize well-defined mucus models and incorporate quantitative in vivo assessments to elucidate the interrelationships between mucus-penetrating ability, cell-specific uptake, and pulmonary delivery efficiency.

ibrotic lesions. The underlying mechanism remains unclear, and the observed behavior is therefore described as pH-dependent rather than actively pH-triggered release. Moreover, as the measurements were obtained from the same release system, independ-

ent batch studies are needed to verify reproducibility and enable robust statistical comparisons. Fluorescence imaging of ICG-labeled DPPC-AS@Liposomes demonstrated pulmonary accumulation, while LC–MS/MS analysis provided direct evidence of AS distribution in tissues. These findings suggest that liposomal encapsulation may improve pulmonary delivery of AS. However, the present study did not distinguish AS distribution between fibrotic and healthy lung tissues or determine its spatial localization within lung sections. Therefore, preferential accumulation in fibrotic lesions cannot be established. Further studies using confocal microscopy and quantitative comparisons of fibrotic and healthy lung tissues are needed to clarify the intrapulmonary distribution and potential lesion-targeting properties of DPPC-AS@Liposomes. The liposomal formulations exhibited sustained and pH-dependent AS release, with kinetic analysis (n = 0.203–0.327) suggesting a substantial contribution of diffusion. PBS at pH 7.4 and 5.5 was used without serum or mucin. The pH 5.5 condition was selected for comparative purposes and does not directly represent the extracellular pH of pulmonary f

In the bleomycin-induced pulmonary fibrosis model, AS@Liposomes attenuated pulmonary injury, inflammatory responses, and collagen deposition more effectively than free AS. Consistent with these findings, the wound-healing assay and fibrosis-related protein and mRNA analyses provided additional evidence for the anti-fibrotic activity of AS@Liposomes. Nevertheless, the L929 fibroblast model does not fully recapitulate the phenotypes and microenvironment of primary pulmonary fibroblasts. Moreover, because mitomycin C was not used in the scratch assay, the observed changes in wound closure may reflect contributions from both cell migration and proliferation. In addition, only selected inflammatory cytokines were examined; therefore, further investigation of TGF-β-related signaling and other fibrosis-associated inflammatory pathways is warranted.

Several limitations of the present study should also be acknowledged. Batch-to-batch reproducibility, long-term formulation stability, and standardized aerosol performance parameters, including MMAD, GSD, and FPF, were not systematically characterized. In addition, the long-term pulmonary safety, immune responses, and potential lipid accumulation following repeated administration remain to be determined. Quantitative assessments of pulmonary fibrosis, such as Ashcroft scoring, hydroxyproline measurement, and quantitative collagen analysis, were also not performed. Future studies incorporating these complementary evaluations, together with cell-specific drug delivery and time-dependent quantitative tissue-distribution or pharmacokinetic analyses, will be important for further elucidating the therapeutic potential and translational applicability of AS-loaded liposomes.

4. Materials and Methods

4.1. Materials

Asiaticoside (AS, purity ≥ 98%), bleomycin sulfate, and formic acid (analytical grade, purity ≥ 98%) were purchased from Macklin Biochemical Co., Ltd. (Shanghai, China). 1,2-Dipalmitoyl-sn-glycero-3-phosphocholine (DPPC, purity ≥ 99%), 1,2-distearoyl-sn-glycero-3-phosphoethanolamine-N-[methoxy(poly-ethylene glycol)-2000] (DSPE-PEG2000, purity ≥ 95%), and cholesterol (purity ≥ 99%) were purchased from Shanghai Fanshu Biotechnology Co., Ltd. (Shanghai, China). 1,2-Dipalmitoyl-sn-glycero-3-phospho-(1′-rac-glycerol) (DPPG, purity ≥ 98%) and 1,2-dioleoyl-3-trimethylammonium-propane (DOTAP, purity ≥ 98%) were purchased from Beijing Push-Tian Biotechnology Co., Ltd. (Beijing, China). Indocyanine green (ICG, purity ≥ 95%) was purchased from Shanghai Eon Chemical Technology Co., Ltd. (Shanghai, China). PBS was purchased from Wuhan Servucebio Technology Co., Ltd. (Wuhan, China).

RPMI-1640 medium, fetal bovine serum (FBS), 0.25% Trypsin-EDTA, and penicillin–streptomycin solution (100×) were purchased from Gibco (Grand Island, NY, USA).

https://doi.org/10.3390/ph19111759

Transwell cell culture inserts (6.5 mm diameter, 0.4 μm pore size) and dialysis bags (molecular weight cut-off: 14,000 Da) were purchased from Shanghai Lanjekko Technology Co., Ltd. (Beijing, China).

Enzyme-linked immunosorbent assay (ELISA) kits for tumor necrosis factor-alpha (TNF-α) and interleukin-6 (IL-6) were purchased from Lianke Biotechnology Co., Ltd. (Hangzhou, China). Hematoxylin–eosin (HE) staining kit and Masson's trichrome staining kit were purchased from Nanjing Jiancheng Bioengineering Institute (Nanjing, China); 4% paraformaldehyde fixation solution and 4′,6-diamidino-2-phenylindole (DAPI) staining solution were purchased from Wuhan Servicebio Technology Co., Ltd. (Wuhan, China).

The mouse fibroblast cell line L929 and the mouse alveolar macrophage cell line MH-S were purchased from Shanghai Fuheng Biotechnology Co., Ltd. (Shanghai, China). Specific pathogen-free (SPF) grade male C57BL/6J mice (6–8 weeks old, 18–20 g) were purchased from Shanghai SLAC Laboratory Animal Co., Ltd. (Shanghai, China).

HPLC-grade acetonitrile was purchased from J&K Scientific (Shanghai, China). Methanol (HPLC grade) was purchased from Merck KGaA (Darmstadt, Germany). The LC-MS/MS system was purchased from Waters Corporation (Milford, MA, USA). Ultrapure water used in all experiments was prepared using a Milli-Q purification system (Merck Millipore, Billerica, MA, USA).

4.2. Methods

4.2.1. Preparation and Characterization of Asiaticoside-Loaded Liposomes (AS@Liposomes)

Preparation and Formulation Optimization of AS@Liposomes

In this study, Asiaticoside-loaded liposomes (AS@Liposomes) were prepared via the thin-film hydration method. The liposomes were prepared using DPPC, DSPE-PEG2000, and cholesterol at a weight ratio of [cholesterol]:[DSPE-PEG2000] = 1:5~1:1 (designated as formulations A1–A5; A0 represented the cholesterol-free control). Three types of phospholipids—DPPC, DPPG, and DOTAP—were employed, ensuring the total mass of phospholipids and cholesterol reached 50 mg. These components were dissolved in a chloroform–methanol mixture (3:1, *v*/*v*) and subjected to rotary evaporation (120 rpm) at specific temperatures (45 °C for DPPC, 40 °C for DPPG, and 35 °C for DOTAP) for at least 1 h to form a uniform lipid film. Subsequently, the film was hydrated with 10 mL of an AS aqueous solution (0.25 mg/mL) in a water bath at the respective phase transition temperatures (60 °C for DPPG, 55 °C for DPPC, and 45 °C for DOTAP) for 30 min. The resulting suspension was further processed using a probe sonicator to reduce the polydispersity. The final AS@Liposomes were stored at 4 °C in light-protected containers for subsequent use.

To prepare indocyanine green (ICG)-labeled fluorescent nanocolloids, an equal amount of ICG was substituted with AS, while the remaining steps were conducted as previously described, ensuring protection from light.

Characterization of the Nanoparticles Size Distribution and Zeta Potential

The AS@Liposomes were dispersed in ultrapure water at the appropriate concentration and sonicated for 2 min to ensure uniform dispersion of the nanoparticles. The samples were then transferred to a clean cuvette for analysis. Dynamic light scattering (DLS) and zeta potential measurements were performed using a Zetasizer Nano ZS90 (Malvern Panalytical, Malvern, UK). Additionally, the zeta potential was determined by placing the samples in a potentiometric cell.

4.2.2. Measurement of Encapsulation Efficiency (EE%) and Drug Loading (DL%)

Establishment of HPLC Conditions and Standard Curves

HPLC conditions: A 4.6 mm × 250 mm, 4.6 μm C18 column was used at a column temperature of 30 °C. The mobile phase ratio was A:B = 70:30 (A, acetonitrile; B, 0.1% formic acid in water) at a flow rate of 1 mL/min. The injection volume was 10 μL, and the detection wavelength was 260 nm.

The AS reference standard was accurately weighed, and we prepared a series of standard solutions with concentrations of 1000 μg/mL, 500 μg/mL, 250 μg/mL, 125 μg/mL, 62.5 μg/mL, 50 μg/mL, 25 μg/mL, 12.5 μg/mL, 6.25 μg/mL, and 5 μg/mL. We filtered these solutions through a 0.22 μm organic-phase microporous membrane and then subjected them to HPLC analysis. We recorded the chromatographic peak areas for each target compound and used the obtained data to construct a standard curve. (Figure S2).

Specificity

To evaluate whether components such as phospholipids, cholesterol, and the buffer system within AS-loaded liposomes (AS@Liposomes) might interfere with the determination of asiaticoside (AS) via high-performance liquid chromatography (HPLC), the researchers assessed the specificity of the analytical method under the established chromatographic conditions. The samples analyzed included AS-loaded liposomes (treated with a 10-fold volume of methanol to precipitate proteins and disrupt the lipid structure), a blank solvent, and an AS standard solution (200 μg/mL). By comparing the retention times and peak shapes of the target analyte across these samples, the researchers examined the potential for interference from excipients or solvents and confirmed that all chromatographic peaks achieved baseline separation. Chromatograms were recorded to facilitate an objective evaluation. (Figure S3).

Precision

Three stock solutions of asiaticoside (AS) at different concentrations (1 mg/mL) were accurately prepared and analyzed according to the aforementioned chromatographic conditions. The samples were filtered through 0.22 μm organic-phase microporous membranes prior to HPLC analysis. Each concentration level was injected six times; the resulting chromatograms were recorded, and the relative standard deviations (RSDs) for retention time and peak area were calculated.

Recovery Rate

To assess the accuracy of the detection method, test solutions with concentrations of 80 μg/mL, 100 μg/mL, and 120 μg/mL—based on a target concentration of 100 μg/mL—were prepared, with three replicates for each concentration. After filtration through a 0.22 μm organic microporous membrane, the solutions were injected into an HPLC system; the peak areas for each compound were recorded, and the recovery rates were calculated.

The standard curve and specificity results are presented in Figures S2 and S3, respectively, while the precision and recovery results are summarized in Tables S3 and S4, respectively.

Determination of Encapsulation Efficiency

Free AS was separated from liposome-encapsulated AS by dialysis using a dialysis membrane. Free AS diffused through the membrane into the external medium, whereas the liposomes were retained within the dialysis bag. The amount of free AS was quantified by HPLC, and the encapsulated AS content was calculated by subtracting the free AS content from the total AS content. AS@Liposomes were prepared in triplicate batches. A 100 μL aliquot of the stock dispersion from each batch was combined with 900 μL of acetonitrile and vortex-mixed for 10 min, followed by centrifugation at 12,000 rpm for 10 min.

The supernatant was collected to assess the loading capacity. Encapsulation efficiency (EE) was calculated as follows:

$$EE(\%) = \frac{M_{total} - M_{free}}{M_{total}} \times 100\% \quad (1)$$

Determination of Drug Loading

AS@Liposomes were prepared under three different conditions, with each batch processed separately. They were freeze-dried using a freeze-dryer, and the resulting freeze-dried AS@Liposomes were weighed. An appropriate amount of acetonitrile was then added to fully dissolve and break the emulsion. Vortexing and ultrasonication assisted in disrupting the preparation's structure during dissolution. The mixture was centrifuged at 12,000 rpm for 10 min, and the supernatant was collected to assess drug loading capacity. The concentration of asiaticoside (AS) was monitored by HPLC after appropriate dilution, and the drug load was calculated based on the obtained results. Drug loading (DL) was calculated as follows:

$$DL(\%) = \frac{M_{encapulated}}{M_{liposomes}} \times 100\% \quad (2)$$

4.2.3. Transmission Electron Microscope (TEM) Imaging

We took a sterilized 200-mesh copper mesh with a carbon support film and applied 10 μL of the AS@Liposome sample, diluted to 0.5 mg/mL with PBS, dropwise. We allowed the sample to be fully adsorbed at room temperature for 2 to 3 min. We removed any excess liquid using dust-free filter paper. Next, we added 5 to 8 μL of a 2% phosphotungstic acid dye solution, with a pH of 7.0 to 7.4, dropwise for 60 to 90 s. We removed the excess dye solution and let it dry naturally at room temperature for 5 to 10 min. We placed the treated copper mesh under a transmission electron microscope (HT7800, Hitachi High-Tech Co., Ltd., Tokyo, Janpan), adjusting the accelerating voltage from low to high magnification at 80 kV. We selected and photographed 5 to 10 typical areas in the field of view where the liposomes were evenly dispersed to observe their microscopic morphology, particle size homogeneity, and dispersion status.

4.2.4. In Vitro Pulmonary Mucus Penetration Assay

Artificial mucus was prepared by mixing 200 mg of porcine gastric mucin, 180 mg of sodium chloride, 4 mg of potassium chloride, and 15 mg of salmon sperm in an appropriate volume of PBS (pH 7.4). Then, 2 μL of Tween 80 was added, and the mixture was brought to a final volume of 20 mL with PBS. The mixture was stirred overnight using a magnetic stirrer to obtain the artificial mucus.

The in vitro mucus permeation properties of various liposomes were assessed using Transwell cell chambers and artificial mucus modeling. To prepare the artificial mucus, 100 μL of it was placed in each donor chamber of a Transwell® (6.5 mm, pore size 0.4 μm), while 800 μL of PBS at pH 7.4 was added to the recipient chamber. The Transwells were then equilibrated at 37 °C for 1 h. Subsequently, 100 μL of free AS, AS@Lipo-DPPC, AS@Lipo-DPPG, and AS@Lipo-DOTAP was introduced to the upper layer of the artificial mucus and incubated in a 37 °C oven. Samples of 100 μL were taken from the receptor chamber at intervals of 0.5, 1, 2, 4, 8, 12, 16, 18, and 24 h, with an equal volume of PBS buffer replenished each time. These samples were dissolved in methanol, and the AS content was measured using HPLC. The results are expressed as the percentage of AS-loaded liposomes that permeated through the artificial mucus layer.

4.2.5. In Vitro Drug Release Behavior Study

The dialysis method was employed to examine the drug release characteristics of AS@Liposomes under varying pH conditions. Quantitative and calibrated concentrations of AS@Liposomes were introduced into a dialysis bag, which was then placed in a 20 mL brown syringe bottle. This bottle contained 10 mL of PBS buffer at pH levels of 7.4 and 5.5. The bottles were shaken in a constant temperature shaker set at 37 °C, and an equal amount of solvent was replenished after sampling at predetermined intervals. High-performance liquid chromatography (HPLC) was used to detect drug release, and the release profile was subsequently plotted.

4.2.6. Investigation of Formulation Stability

A 100 μL sample of prepared AS@Liposomes was added to 1 mL of RPMI-1640 medium with 10% serum and stored for 7 days. The average particle size, zeta potential, and PDI of the nanomicelles were measured daily to evaluate the stability of the preparation during storage.

4.3. In Vitro Anti-Pulmonary Fibrosis Activity Evaluation

4.3.1. Cell Culture

Cell Resuscitation

We transferred the necessary consumables to a biosafety cabinet and activated a UV light for pre-sterilization. We retrieved the mouse fibroblasts (L929) from the cryostat tubes and gently shook them at 37 °C until thawed. Once thawed, we transferred the cell suspension to a 15 mL centrifuge tube within the biosafety cabinet and diluted it by adding 5 mL of culture medium. We centrifuged the mixture at 1000 rpm for 5 min and then discarded the supernatant. We added 1 mL of complete medium to resuspend the cells. We placed the resuspended cells in a Petri dish or culture flask, added an appropriate amount of complete culture medium, and incubated them. We changed the medium or passaged the cells at suitable intervals.

Cell Culture and Passage

To observe cell growth under a microscope, we ensured that the culture background was clean and that the cells exhibited good morphology. When cell density surpassed 80%, we passaged the cells. First, we sterilized the biosafety cabinet and all necessary consumables. In the cabinet, we discarded the original medium and washed the cells 2 to 3 times with PBS buffer. We added an appropriate amount of trypsin containing EDTA and incubated the cells for 30 to 60 s. Digestion was stopped when most cells appeared rounded under a microscope by adding an appropriate amount of complete medium. We pipetted the cell suspension, collected the cells by gently pipetting, and transferred the suspension to a centrifuge tube. We centrifuged at 1000 rpm for 5 min and discarded the supernatant. We resuspended the cells by adding an appropriate amount of complete medium, then diluted the cells to the desired volume, and transferred them to a new dish or flask. We added complete medium as needed and recorded the relevant information. Finally, we placed the new dishes or flasks in an incubator for further incubation.

Cell Cryopreservation

The cell digestion process aligns with the procedures outlined before. Cell Culture and Transfection. After being collected via centrifugation, the cells were gently resuspended by adding an appropriate volume of cryopreservation solution. The cell suspension was then distributed into cryopreservation tubes. The cells underwent a programmed cooling process before being stored in either liquid nitrogen or a −80 °C freezer.

4.3.2. Cellular Uptake

The uptake of AS@Liposomes by mouse alveolar macrophages (MH-s) was examined using laser confocal microscopy (Leica STELLARIS, Leica Camera AG, Wetzlar, Germany). The ICG content in the fluorescently labeled preparations (AS@DPPC-ICG, AS@DPPG-ICG, AS@DOTAP-ICG) was quantified with a UV spectrophotometer (Varioskan LUX, Thermo Fisher Scientific Inc., Waltham, MA, USA) to ensure that each group had an ICG concentration of 20 μg/mL at the time of drug administration. Cells in the logarithmic growth phase were inoculated at a density of 1×10^6 cells per dish in laser confocal culture dishes and cultured for 24 h to allow for cell attachment. At the time of drug administration, the original medium was discarded, and the drug was added according to the designated groups and time points to maintain consistency throughout the experiment. After drug administration, the medium was removed, and the cells were washed with PBS at least three times. Next, 4% paraformaldehyde was added for fixation for 30 min. After another wash, DAPI staining solution was applied for 10 min, followed by a final wash. Once washing was complete, the washings were discarded, and 1 mL of PBS was added for observation under a laser confocal microscope.

The experimental groupings were organized as follows: In the free-ICG group, cells were exposed to a medium with free-ICG for 1, 2, and 4 h. The fluorescently labeled DPPC-loaded group (AS@DPPC-ICG) involved treating cells with AS@DPPC-ICG for the same durations. Similarly, the fluorescently labeled negative phospholipid DPPG-loaded group (AS@DPPG-ICG) had cells treated with AS@DPPG-ICG for 1, 2, and 4 h. Lastly, the fluorescently labeled positive phospholipid DOTAP-loaded group (AS@DOTAP-ICG) also involved treating cells for 1, 2, and 4 h with AS@DOTAP-ICG.

4.3.3. Establishment of TGF-β1-Induced Mouse Fibroblast Activation Model

L929 cells in the logarithmic growth phase were inoculated into cell culture plates at an appropriate density and incubated in a 37 °C, 5% CO_2 environment until 70% to 80% confluence was achieved. The original medium was then discarded, and the cells were synchronized by a 24 h starvation treatment using serum-free medium. Subsequently, a complete medium containing TGF-β1 (10 ng/mL) was added for induction, while a blank control group received only serum-free medium. The culture was maintained for 48 h. The success of the lung fibrosis cell model was verified by detecting the expression of fibrosis-related proteins, such as α-SMA and Collagen I. Cells underwent an additional 24 h starvation with serum-free medium to ensure synchronization.

4.3.4. Wound Healing Assay

The DPPC-based asiaticoside-loaded liposomes (DPPC-AS@Liposomes), selected based on the preliminary formulation screening results, were used in the subsequent in vitro anti-fibrotic experiments. To prepare L929 cells for the experiment, we began by taking cells in the logarithmic growth phase and creating a single-cell suspension following trypsin digestion. We inoculated these cells into 6-well plates at an appropriate density and incubated them at 37 °C with 5% CO_2 until they reached 80–90% confluence. Using a sterile 10 μL pipette tip held perpendicular to the plate surface, we made three parallel straight scratches in the center of the cell monolayer in each well, ensuring that the scratches extended across the entire well bottom for consistency. We gently washed the cells three times with PBS buffer to remove any floating cells and debris and then added the appropriate serum-containing medium to continue culturing. At 0 h, 24 h, and 48 h, we observed and photographed the scratched areas using an inverted microscope (DMi8, Leica Camera AG, Wetzlar, Germany). We set up three duplicate wells for each experimental group to minimize error. We measured the average width of the scratches at each

time point using the image analysis software ImageJ (version 1.54p). We calculated the cell migration rate using the following formula:

$$Migration\ rate = \frac{W_0 - W_t}{W_0} \times 100\% \quad (3)$$

4.3.5. Western Blot Assay

Proteins were extracted from cells using RIPA lysis buffer (Beyotime Institute of Biotechnology, Shanghai, China). The same amount of protein was separated on a 10% SDS-PAGE gel and then transferred onto PVDF membranes (Bio-Rad Laboratories, Inc., Hercules, CA, USA). After blocking with 5% nonfat milk, the membranes were incubated with primary antibodies against α-SMA (#14968, 1:1000, Cell Signalling Technology, CST, Beverly, MA, USA), fibronectin (ab2413, 1:1000, Abcam, Cambridge, UK) and GAPDH (#5174, 1:1000, CST) at 4 °C overnight. Then, the membranes were incubated with corresponding peroxidase-linked secondary antibodies at room temperature for 1 h. Signal detection was performed using an ECL system (Millipore, Billerica, MA, USA).

4.3.6. Reverse Transcription-Quantitative Polymerase Chain Reaction (RT-qPCR)

Total RNAs were extracted from lung tissues using TRIzol (Invitrogen; Thermo Fisher Scientific, Inc., Waltham, MA, USA) according to the manufacturer's protocol. PrimeScript RT reagent kit (Takara Bio, Inc., Otsu, Japan) was used for transcription from RNA to cDNA. qPCR was performed in a final volume of 20 μL using a 2× SYBR Green qPCR kit (Takara Bio, Inc., Otsu, Japan). The expression levels of TGF-β1, collagen I and collagen III were calculated using the $2^{-\Delta\Delta Ct}$ method with GAPDH as an internal control for normalization.

4.4. In Vivo Pharmacodynamic Evaluation

4.4.1. Establishment of Bleomycin-Induced Mouse Model of Pulmonary Fibrosis

Male C57BL/6J mice, aged 6–8 weeks and weighing 18–20 g, were selected for the study. Anesthesia was administered, followed by an intratracheal aerosol microsprayer of bleomycin sulfate at a dose of 2 mg/kg to induce a pulmonary fibrosis model. After the procedure, the mice were placed in a rat cage and monitored until their cardiopulmonary activity, feeding, and water intake returned to normal upon awakening. Post-modeling, the mice were observed for changes in diet and body weight and underwent pathological diagnosis to assess the success of the modeling.

4.4.2. Randomization, Blinding, and Animal Welfare

Before treatment, mice were randomly allocated to the experimental groups, with 10 animals assigned to each group. Histological evaluation was performed according to predefined pathological assessment criteria; however, the histological analysis was not performed in a blinded manner. Humane endpoints were predefined in accordance with the approved animal-use protocol, and animals were monitored throughout the experimental period for changes in general health, activity, body condition, and feeding status. No animals met the predefined exclusion criteria during the study, and no mortality occurred during the experimental period. Therefore, all 10 animals in each group were included in the final analysis.

4.4.3. Investigation of In Vivo Biodistribution

The distribution of the drug in mice was assessed using small-animal in vivo imaging. Six C57 mice, which were successfully modeled, were randomly chosen and divided into groups based on IVIS imaging results and body weight (). Each group received a drug

concentration of 0.4 mg/kg, measured by ICG content, with a nebulized inhalation drop volume of 25 μL per dose. The groupings were as follows: $n = 3$

Aerosolized free-ICG group (free-ICG);
Aerosolized AS@Liposomes-ICG group (AS@Liposomes-ICG).

The distribution of fluorescent markers in mice was photographed using the IVIS imaging system (IVIS Lumina III, PerkinElmer, Inc., Shanghai, China) at 15 min, 30 min, 1 h, 2 h, 4 h, 6 h and 8 h post-drug administration. The mice were euthanized 24 h after drug administration, and their organs were removed for ex vivo imaging.

4.4.4. In Vivo Anti-Fibrotic Efficacy Evaluation

Grouping and Administration Protocol

Male C57BL/6J mice (6–8 weeks old, 18–20 g) were randomly assigned to four experimental groups ($n = 10$): control, model, free AS, and AS@Liposomes. Both free AS and AS@Liposomes were administered at an AS-equivalent dose of 40 mg/kg, once every two days, for a duration of 14 days. Pulmonary drug delivery was performed via an intratracheal aerosol microsprayer (YAN30012, Shanghai Yuyan Instruments Co., Ltd., Shanghai, China), through which 25 μL of the formulation was delivered directly into the trachea to achieve controlled and reproducible pulmonary dosing. Briefly, mice were anesthetized to a depth sufficient to prevent tongue retraction. Following immobilization on a dedicated platform, the vocal folds were visualized under a cold light source. A volume of 25 μL of the drug formulation was rapidly instilled into the trachea. The success of the administration was confirmed by a transient increase in respiratory rate and the presence of audible pulmonary wet rales.

Data Collection and Animal Sampling During Administration

After initiating drug administration, we observed the mice's overall condition at a consistent time each day. We recorded their mental status, diet and water intake, activity levels, fur color, and any deaths. We weighed the mice every two days using an electronic balance (MX105DU/A, Mettler-Toledo Group, Zurich, Switzerland) to calculate the rate of body mass change. Before concluding the drug administration cycle, we tested the mice for relevant indices based on experimental needs. Throughout the process, we meticulously recorded and organized the experimental data, promptly excluding any abnormal mice. At the end of the treatment, we euthanized the mice and collected their serum, bronchial lavage fluid, and major organs (heart, liver, spleen, kidneys, lungs). We stored these samples appropriately, following the requirements of subsequent experimental protocols.

Hematoxylin–Eosin (HE) and Masson Staining

The lung tissue samples were fixed with 4% paraformaldehyde. Following fixation, the samples underwent gradient dehydration, paraffin embedding, and serial sectioning. They were then stained with hematoxylin–eosin (HE) and Masson's trichrome in sequence. After dehydration, transparency, and sealing with neutral gum, the samples were examined under a light microscope (DMi1, Leica Camera AG, Wetzlar, Germany) to observe the pathological morphology of the lung tissues and collagen fiber deposition.

Detection of Inflammatory Factors in Bronchoalveolar Lavage Fluid (BALF) and Serum.

Alveolar lavage fluid supernatant and serum samples were collected, and an enzyme-linked immunosorbent assay (ELISA) was employed to measure the concentrations of TNF-α, IL-6, and other inflammatory factors. Following sample dilution, a standard gradient was prepared, and the samples were incubated. The plate was then washed, en-

zyme reagent was added, color was developed, and the reaction was terminated according to the instruction manual. After these steps, absorbance was measured at the specified wavelength using an enzyme marker. The concentration of each inflammatory factor was calculated using the standard curve to assess the expression levels of these factors in the alveolar lavage fluid and serum.

4.4.5. Evaluation of Biological Safety

Paraffin sections of major organs (heart, liver, spleen, kidneys) from mice in each group were prepared for HE staining to assess the pathological status of these organs. Concurrently, the weight changes in the mice during the treatment period were monitored and recorded. At the end of the treatment, serum was collected, and blood biochemical indices were tested to evaluate the liver and kidney functions, as well as the nutritional status, of the mice. These factors were integrated to assess the biocompatibility and safety of the preparation.

4.5. Statistical Analysis

The data is presented as the mean ± standard deviation (SD). Statistical significance was assessed using Student's *t*-test or one-way ANOVA with GraphPad Prism 8.0. The difference was considered statistically significant at $p < 0.05$. Statistical significance is indicated as * $p < 0.05$, ** $p < 0.01$, and *** $p < 0.001$.

5. Conclusions

In this study, pH-responsive asiaticoside liposomes (AS@Liposomes) with tunable surface charges were successfully constructed for pulmonary fibrosis therapy. The optimized DPPC-based liposomes exhibited high encapsulation efficiency, uniform size, excellent colloidal stability, pH-responsive drug release, strong mucus penetration, and reduced alveolar macrophage uptake. In vitro, AS@Liposomes significantly inhibited TGF-β1-induced fibroblast activation and migration. In bleomycin-induced pulmonary fibrosis mice, inhaled AS@Liposomes effectively alleviated body weight loss, attenuated lung injury and collagen deposition, and suppressed TNF-α and IL-6 overexpression, with superior efficacy to Free AS and favorable biosafety. Overall, these findings demonstrate that the inhalable AS@Liposome system can improve the pulmonary delivery and anti-fibrotic efficacy of asiaticoside, highlighting its potential as a pulmonary nanodelivery strategy for the treatment of pulmonary fibrosis.

Supplementary Materials: The following supporting information can be downloaded at https://www.mdpi.com/article/10.3390/ph19111759/s1, Figure S1: Physicochemical properties of DPPC/DPPG/DOTAP liposomes at different formulations (A0–A5); Figure S2: Standard curve for asiaticoside (5–1000 μg/mL); Figure S3: Results of the specificity investigation, including the solvent peak and asiaticoside; Table S1: Kinetic parameters of drug release from different liposome formulations at pH 7.4 and pH 5.5; Table S2: Encapsulation efficiency (EE%) and drug loading (DL%) of liposomal formulations A0–A5 based on DPPC, DPPG, and DOTAP; Table S3: Precision evaluation of the HPLC method for asiaticoside determination ($n = 3$); Table S4: Recovery of asiaticoside (AS) determined by the HPLC method ($n = 3$).

Author Contributions: Conceptualization, J.Z., X.F.; methodology, J.Z.; validation, J.Z., X.F. and X.T.; investigation, J.Z., X.F. and X.T.; resources, X.C.; data curation, J.Z. and X.T.; writing—original draft preparation, J.Z. and X.F.; visualization, J.Z.; supervision, X.C.; project administration, X.C.; funding acquisition, X.C. All authors have read and agreed to the published version of the manuscript.

Funding: This study was financially supported by the Zhejiang Province Traditional Chinese Medicine Science and Technology Plan Project (Grant No. 2024ZR025).

Institutional Review Board Statement: The animal study protocol was approved by the Committee on Ethics of Medicine, Zhejiang Chinese Medicine University (IACUC-20240401-16, 1 April 2024).

Informed Consent Statement: Not applicable.

Data Availability Statement: The original contributions presented in this study are included in the article. Further inquiries can be directed to the corresponding author.

Acknowledgments: Artificial intelligence-assisted tools were used in the preparation of this manuscript for language polishing, the creation of a graphical abstract, and minor grammatical revisions. No artificial intelligence tools were employed in the research design, data analysis, or interpretation of the results. The authors confirm that the scientific content and conclusions of this study are entirely their own work.

Conflicts of Interest: The authors declare no conflicts of interest.

Abbreviations

The following abbreviations are used in this manuscript:

PF	Pulmonary fibrosis
AS	Asiaticoside
TGF-β1	Transforming growth factor-beta 1
TNF-α	Tumor necrosis factor-alpha
α-SMA	Alpha-smooth muscle actin
IL-6	Interleukin-6
DPPC	1,2-Dipalmitoyl-sn-glycero-3-phosphocholine
DPPG	1,2-Dipalmitoyl-sn-glycero-3-phospho-(1′-rac-glycerol)
DOTAP	1,2-Dioleoyl-3-trimethylammonium-propane
DSPE-PEG2000	1,2-Distearoyl-sn-glycero-3-phosphoethanolamine-N-[methoxy (polyethylene glycol)-2000]
ICG	Indocyanine green
FBS	Fetal bovine serum
ELISA	Enzyme-linked immunosorbent assay
HE	Hematoxylin–eosin
DAPI	4′,6-Diamidino-2-phenylindole
SPF	Specific pathogen-free
HPLC	High-performance liquid chromatography
DLS	Dynamic light scattering
TEM	Transmission electron microscope
EE	Encapsulation efficiency
DL	Drug loading
PDI	Polydispersity index
BLM	Bleomycin
BALF	Bronchoalveolar lavage fluid
ALT	Alanine transaminase
AST	Aspartate transaminase
CREA	Creatinine
BUN	Blood urea nitrogen

References

1. Cha, S.; Lee, J.; Jang, J.; Kim, Y.; Han, D.; Hong, S.H.; Kim, S.J.; Lee, D.H.; Ma, C.H.; Lee, H.P.; et al. Exosomes from Human Embryonic Stem Cell-Derived Mesenchymal Stem Cells Protect Lung Epithelium and Attenuate Fibrosis. *Int. J. Stem Cells* **2026**, *19*, 66–82. https://doi.org/10.15283/ijsc25091.

2. Maher, T.M.; Bendstrup, E.; Dron, L.; Langley, J.; Smith, G.; Khalid, J.M.; Patel, H.; Kreuter, M. Global incidence and prevalence of idiopathic pulmonary fibrosis. *Respir. Res.* **2021**, *22*, 197. https://doi.org/10.1186/s12931-021-01791-z.
3. Martinez, F.J.; Collard, H.R.; Pardo, A.; Raghu, G.; Richeldi, L.; Selman, M.; Swigris, J.J.; Taniguchi, H.; Wells, A.U. Idiopathic pulmonary fibrosis. *Nat. Rev. Dis. Primers* **2017**, *3*, 17074. https://doi.org/10.1038/nrdp.2017.74.
4. Sauleda, J.; Núñez, B.; Sala, E.; Soriano, J.B. Idiopathic Pulmonary Fibrosis: Epidemiology, Natural History, Phenotypes. *Med. Sci.* **2018**, *6*, 110. https://doi.org/10.3390/medsci6040110.
5. Dong, R.; Liu, M.; Huang, X.X.; Liu, Z.; Jiang, D.Y.; Xiao, H.J.; Geng, J.; Ren, Y.H.; Dai, H.P. Water-Soluble C(60) Protects Against Bleomycin-Induced Pulmonary Fibrosis in Mice. *Int. J. Nanomed.* **2020**, *15*, 2269–2276. https://doi.org/10.2147/ijn.S214056.
6. Guillen-Guio, B.; Marcelino-Rodriguez, I.; Lorenzo-Salazar, J.M.; Leavy, O.C.; Allen, R.J.; Pompa-Mera, E.N.; Riancho, J.A.; Rojas-Martinez, A.; Lapunzina, P.; Carracedo, Á.; et al. Polygenic risk of idiopathic pulmonary fibrosisandCOVID-19severity. MedRxiv, 2023.06.12.23291269,.https://doi.org/10.1101/2023.06.12.23291269.
7. Bonella, F.; Spagnolo, P.; Ryerson, C. Current and Future Treatment Landscape for Idiopathic Pulmonary Fibrosis. *Drugs* **2023**, *83*, 1581–1593. https://doi.org/10.1007/s40265-023-01950-0.
8. Shen, H.; Zhang, N.; Liu, Y.; Yang, X.; He, Y.; Li, Q.; Shen, X.; Zhu, Y.; Yang, Y. The Interaction Between Pulmonary Fibrosis and COVID-19 and the Application of Related Anti-Fibrotic Drugs. *Front. Pharmacol.* **2021**, *12*, 805535. https://doi.org/10.3389/fphar.2021.805535.
9. Kim, M.E.; Lim, Y.; Lee, J.S. Mitochondrial Dysfunction and Metabolic Reprogramming in Chronic Inflammatory Diseases: Molecular Insights and Therapeutic Opportunities. *Curr. Issues Mol. Biol.* **2025**, *47*, 1042. https://doi.org/10.3390/cimb47121042.
10. Maus, M.; López-Polo, V.; Mateo, L.; Lafarga, M.; Aguilera, M.; De Lama, E.; Meyer, K.; Sola, A.; Lopez-Martinez, C.; López-Alonso, I.; et al. Iron accumulation drives fibrosis, senescence and the senescence-associated secretory phenotype. *Nat. Metab.* **2023**, *5*, 2111–2130. https://doi.org/10.1038/s42255-023-00928-2.
11. Bayraktar, E.A.; Salvatore, M. The intersection of liver cirrhosis and pulmonary fibrosis. *J. Transl. Med.* **2025**, *24*, 223. https://doi.org/10.1186/s12967-025-07449-4.
12. Saito, A.; Horie, M.; Micke, P.; Nagase, T. The Role of TGF-β Signaling in Lung Cancer Associated with Idiopathic Pulmonary Fibrosis. *Int. J. Mol. Sci.* **2018**, *19*, 3611. https://doi.org/10.3390/ijms19113611.
13. Cheng, D.; Xu, Q.; Wang, Y.; Li, G.; Sun, W.; Ma, D.; Zhou, S.; Liu, Y.; Han, L.; Ni, C. Metformin attenuates silica-induced pulmonary fibrosis via AMPK signaling. *J. Transl. Med.* **2021**, *19*, 349. https://doi.org/10.1186/s12967-021-03036-5.
14. Park, S.J.; Ryu, H.W.; Kim, J.H.; Hahn, H.J.; Jang, H.J.; Ko, S.K.; Oh, S.R.; Lee, H.J. Daphnetin Alleviates Bleomycin-Induced Pulmonary Fibrosis through Inhibition of Epithelial-to-Mesenchymal Transition and IL-17A. *Cells* **2023**, *12*, 2795. https://doi.org/10.3390/cells12242795.
15. Liu, X.; Lu, F.; Chen, X. Examination of the role of necroptotic damage-associated molecular patterns in tissue fibrosis. *Front. Immunol.* **2022**, *13*, 886374. https://doi.org/10.3389/fimmu.2022.886374.
16. Yao, M.; Liu, Z.; Zhao, W.; Song, S.; Huang, X.; Wang, Y. Ferroptosis in idiopathic pulmonary fibrosis: Mechanisms, impact, and therapeutic opportunities. *Front. Immunol.* **2025**, *16*, 1567994. https://doi.org/10.3389/fimmu.2025.1567994.
17. Majdalawieh, A.F.; Yousef, S.M.; Abu-Yousef, I.A.; Nasrallah, G.K. Immunomodulatory and Anti-Inflammatory Effects of Berberine in Lung Tissue and its Potential Application in Prophylaxis and Treatment of COVID-19. *Front. Biosci.* **2022**, *27*, 166. https://doi.org/10.31083/j.fbl2705166.
18. Li, Y.; Yang, F.; Yuan, M.; Jiang, L.; Yuan, L.; Zhang, X.; Li, Y.; Dong, L.; Bao, X.; Yin, S. Synthesis and evaluation of asiatic acid derivatives as anti-fibrotic agents: Structure/activity studies. *Steroids* **2015**, *96*, 44–49. https://doi.org/10.1016/j.steroids.2014.11.001.
19. Wu, Z.; Yang, L.; Wang, R.; Yang, J.; Liang, P.; Ren, W.; Yu, H. Exploring the Mechanism of Asiatic Acid against Atherosclerosis Based on Molecular Docking, Molecular Dynamics, and Experimental Verification. *Pharmaceuticals* **2024**, *17*, 969. https://doi.org/10.3390/ph17070969.
20. Sun, M.; Wang, Q.; Huang, J.; Sun, Q.; Yu, Q.; Liu, X.; Liu, Z. Asiatic acid induces ferroptosis of RA-FLS via the Nrf2/HMOX1 pathway to relieve inflammation in rheumatoid arthritis. *Int. Immunopharmacol.* **2024**, *137*, 112394. https://doi.org/10.1016/j.intimp.2024.112394.
21. Li, Z.; Xiao, X.; Yang, M. Asiatic Acid Inhibits Lipopolysaccharide-Induced Acute Lung Injury in Mice. *Inflammation* **2016**, *39*, 1642–1648. https://doi.org/10.1007/s10753-016-0398-z.
22. Guo, W.; Liu, W.; Jin, B.; Geng, J.; Li, J.; Ding, H.; Wu, X.; Xu, Q.; Sun, Y.; Gao, J. Asiatic acid ameliorates dextran sulfate sodium-induced murine experimental colitis via suppressing mitochondria-mediated NLRP3 inflammasome activation. *Int. Immunopharmacol.* **2015**, *24*, 232–238. https://doi.org/10.1016/j.intimp.2014.12.009.

23. Wang, J.; Ma, C.; Guo, C.; Yuan, R.; Zhan, X. CTG-loaded liposomes as an approach for improving the intestinal absorption of asiaticoside in Centella Total Glucosides. *Int. J. Pharm.* **2016**, *509*, 296–304. https://doi.org/10.1016/j.ijpharm.2016.05.044.
24. Zheng, F.; Li, R.; He, Q.; Koral, K.; Tao, J.; Fan, L.; Xiang, R.; Ma, J.; Wang, N.; Yin, Y.; et al. The electrostimulation and scar inhibition effect of chitosan/oxidized hydroxyethyl cellulose/reduced graphene oxide/asiaticoside liposome based hydrogel on peripheral nerve regeneration in vitro. *Mater. Sci. Eng. C Mater. Biol. Appl.* **2020**, *109*, 110560. https://doi.org/10.1016/j.msec.2019.110560.
25. Feng, L.; Liu, Y.; Chen, Y.; Xiang, Q.; Huang, Y.; Liu, Z.; Xue, W.; Guo, R. Injectable Antibacterial Hydrogel with Asiaticoside-Loaded Liposomes and Ultrafine Silver Nanosilver Particles Promotes Healing of Burn-Infected Wounds. *Adv. Healthc. Mater.* **2023**, *12*, e2203201. https://doi.org/10.1002/adhm.202203201.
26. Sharmila, A.; Bhadra, P.; Kishore, C.; Selvaraj, C.I.; Kavalakatt, J.; Bishayee, A. Nanoformulated Terpenoids in Cancer: A Review of Therapeutic Applications, Mechanisms, and Challenges. *Cancers* **2025**, *17*, 3013. https://doi.org/10.3390/cancers17183013.
27. Maritim, S.; Boulas, P.; Lin, Y. Comprehensive analysis of liposome formulation parameters and their influence on encapsulation, stability and drug release in glibenclamide liposomes. *Int. J. Pharm.* **2021**, *592*, 120051. https://doi.org/10.1016/j.ijpharm.2020.120051.
28. Carneiro, S.P.; Greco, A.; Chiesa, E.; Genta, I.; Merkel, O.M. Shaping the future from the small scale: Dry powder inhalation of CRISPR-Cas9 lipid nanoparticles for the treatment of lung diseases. *Expert. Opin. Drug Deliv.* **2023**, *20*, 471–487. https://doi.org/10.1080/17425247.2023.2185220.
29. Gref, R.; Lück, M.; Quellec, P.; Marchand, M.; Dellacherie, E.; Harnisch, S.; Blunk, T.; Müller, R.H. 'Stealth' corona-core nanoparticles surface modified by polyethylene glycol (PEG): Influences of the corona (PEG chain length and surface density) and of the core composition on phagocytic uptake and plasma protein adsorption. *Colloids Surf. B Biointerfaces* **2000**, *18*, 301–313. https://doi.org/10.1016/s0927-7765(99)00156-3.
30. Bakker-Woudenberg, I.A.; Schiffelers, R.M.; Storm, G.; Becker, M.J.; Guo, L. Long-circulating sterically stabilized liposomes in the treatment of infections. *Methods Enzymol.* **2005**, *391*, 228–260. https://doi.org/10.1016/s0076-6879(05)91014-8.
31. Tong, M.; Kuang, X.; Jiang, Q.; Li, G.; Jin, L.; Ye, Y.; Pan, Y.; Zhu, Y.; Mou, X.; Mao, Z.; et al. Spore-inspired inhalation drug delivery system for asthma therapy. *Bioact. Mater.* **2025**, *53*, 801–818. https://doi.org/10.1016/j.bioactmat.2025.07.045.
32. Keshavarz, A.; Kadry, H.; Alobaida, A.; Ahsan, F. Newer approaches and novel drugs for inhalational therapy for pulmonary arterial hypertension. *Expert. Opin. Drug Deliv.* **2020**, *17*, 439–461. https://doi.org/10.1080/17425247.2020.1729119.
33. Fu, W.; Yao, Y.; Li, Y. Novel Carbon Dots Nanomaterials for the Precision Diagnosis and Treatment of Acute Lung Injury and Acute Respiratory Distress Syndrome: Mechanisms and Applications. *Int. J. Nanomed.* **2026**, *21*, 587763. https://doi.org/10.2147/ijn.S587763.
34. Zhou, T.; Wang, C.; Liu, Y.; Song, Z.; Wei, Y.; Wang, R.; Sun, C.; Li, R.; Zhao, M.; Hou, S.; et al. Nebulized macrophage membrane-engineered triptolide liposomes for Siglec-10/CD24-mediated therapeutic targeting in lung cancer. *Int. J. Pharm. X* **2025**, *10*, 100453. https://doi.org/10.1016/j.ijpx.2025.100453.
35. Wang, Y.; Xuan, W.; Mao, C.; Liu, Y. Inhalable nucleic acid therapeutics for chronic pulmonary disease: Progress, challenges, and prospects. *Acta Biomater.* **2025**, *204*, 187–204. https://doi.org/10.1016/j.actbio.2025.07.068.
36. Jones, K.M.; Randtke, E.A.; Howison, C.M.; Cárdenas-Rodríguez, J.; Sime, P.J.; Kottmann, M.R.; Pagel, M.D. Measuring extracellular pH in a lung fibrosis model with acidoCEST MRI. *Mol. Imaging Biol.* **2015**, *17*, 177–184. https://doi.org/10.1007/s11307-014-0784-6.
37. Kottmann, R.M.; Kulkarni, A.A.; Smolnycki, K.A.; Lyda, E.; Dahanayake, T.; Salibi, R.; Honnons, S.; Jones, C.; Isern, N.G.; Hu, J.Z.; et al. Lactic acid is elevated in idiopathic pulmonary fibrosis and induces myofibroblast differentiation via pH-dependent activation of transforming growth factor-β. *Am. J. Respir. Crit. Care Med.* **2012**, *186*, 740–751. https://doi.org/10.1164/rccm.201201-0084OC.
38. Sanchez, A.; Loughrey, D.; Echeverri, E.S.; Huayamares, S.G.; Radmand, A.; Paunovska, K.; Hatit, M.; Tiegreen, K.E.; Santangelo, P.J.; Dahlman, J.E. Substituting Poly(ethylene glycol) Lipids with Poly(2-ethyl-2-oxazoline) Lipids Improves Lipid Nanoparticle Repeat Dosing. *Adv. Healthc. Mater.* **2024**, *13*, e2304033. https://doi.org/10.1002/adhm.202304033.

39. Stevens, C.A.; Sevarika, B.; Wilson, B.K.; Wang, C.M.; Cárcamo-Oyarce, G.; Romeo, J.; Degen, G.; Kassis, T.; Lehr, C.M.; Carrier, R.L.; et al. Polymer Blend Controls Nanoparticles' Surface Charge for Improved Mucus Penetration and Epithelial Cell Adhesion. *Nano Lett.* **2025**, *25*, 16963–16969. https://doi.org/10.1021/acs.nanolett.5c02487.
40. Haney, M.J.; Zhao, Y.; Fallon, J.K.; Yue, W.; Li, S.M.; Lentz, E.E.; Erie, D.; Smith, P.C.; Batrakova, E.V. Extracellular Vesicles as Drug Delivery System for Treatment of Neurodegenerative Disorders: Optimization of the Cell Source. *Adv. Nanobiomed Res.* **2021**, *1*, 202100064. https://doi.org/10.1002/anbr.202100064.

Disclaimer/Publisher's Note: The statements, opinions and data contained in all publications are solely those of the individual author(s) and contributor(s) and not of MDPI and/or the editor(s). MDPI and/or the editor(s) disclaim responsibility for any injury to people or property resulting from any ideas, methods, instructions or products referred to in the content.